An unreported precipitate orientation relationship in Al-Zn-Mg based alloys

Artenis Bendo[1*], Kenji Matsuda[1], Adrian Lervik[2], Tomohito Tsuru[3], Katsuhiko Nishimura[1], Norio Nunomura[1], Randi Holmestad[2], Calin D. Marioara[4], Kazuyuki Shimizu[5], Hiroyuki Toda[5] and Masatake Yamaguchi[3]

[1] Graduate School of Science and Engineering, University of Toyama, 3190 Gofuku, Toyama 930-8555, Japan
[2] Department of Physics, Norwegian University of Science and Technology (NTNU), 7491 Trondheim, Norway
[3] Japan Atomic Energy Agency, Tokai, Ibaraki 319-1195, Japan
[4] SINTEF Industry, 7465 Trondheim, Norway
[5] Department of Mechanical Engineering, Kyushu University, Fukuoka 819-0395, Japan

Characterization of precipitates in Al-Zn-Mg alloys, using a combination of electron diffraction, bright field transmission electron microscopy and atomic scale scanning transmission electron microscopy imaging revealed the presence of an unreported η_{13} orientation relationship between the η-$MgZn_2$ phase and the Al lattice with the following orientation relationship $(0001)_\eta \parallel (120)_{Al}$ and $(2\bar{1}\bar{1}0)_\eta \parallel (001)_{Al}$, plate on $(120)_{Al}$. The precipitate interfaces were observed and analyzed along two projections 90° to one-another. The precipitate coarsening was through the common thickening ledge mechanism. The ledges were significantly stepped along one lateral direction, while being absent in the other direction. An interface relaxation model using density functional theory was carried out to explain the precipitate behavior.

Keywords: Aluminum alloys, Precipitation, Microstructure, $MgZn_2$, Transmission electron microscopy, Density functional theory

* Corresponding author: artibendo@gmail.com; d1771103@ems.u-toyama.ac.jp

Introduction

Al-Zn-Mg-(Cu) alloys are important in the aviation and automotive industry due to their high strength to weight ratio [1]. High amounts of Zn, Mg and Cu solute atoms together with vacancies form the chemical driving force resulting in age-hardening through precipitation, after quenching from solutionizing temperature [2]. Solid solution decomposition starts with formation of volumes rich in solute atoms termed GP(I) and GP(II) zones [3]. GP(I) zones are created by substitution and ordering of solute atoms along $\langle 100 \rangle_{Al}$ in the Al lattice [3]. Similar diffraction patterns from zones in different Al alloy systems imply similar nature of ordering of solute atoms [4]. GP(II) zones are described as zinc-rich layers on $\{111\}_{Al}$ planes, that have been observed along $\langle 110 \rangle_{Al}$ when the alloy was quenched from solid solution temperatures above 450°C [3, 5, 6]. The decomposition mechanisms are proposed to occur via different routes. Ageing below GP-zones solvus lines for alloys with Zn/Mg ratio over 2 decomposes the solid solution mainly through: SSSS → GP(I) → η' → η_2 [6, 7]. Solution heat treatment above 450°C increases the vacancy concentration, which upon quenching increases the probability of formation of vacancy rich clusters (VRC) which then serve as nucleation centers for successive phases: SSSS → VRC → high aspect ratio GP(II) → η' → η_2 [3]. Ageing above the GP-zone solvus promotes the formation of η_1 orientation relationships between the

$MgZn_2$/Al lattice [8, 9]. The GP-zone formation temperature limit is in the range of 120-150°C for commonly used 7xxx Al series [10,11,16] When the alloys is deformed prior to ageing heat treatment, this promotes η phases with rod/lath-shaped morphology denoted η_4 to η_8, due to heterogeneous nucleation on line defects [12]. The equilibrium phase for this system is the Laves η ($MgZn_2$) with space group $P6_3/mmc$ and lattice parameters a = 0.522 nm and c = 0.856 nm [13,14]. All η-type stable precipitates imaged so far by atomic resolution high angle annular dark-field scanning transmission electron microscopy (HAADF-STEM) have shown to have the equilibrium η crystal structure but with different orientations in respect to the Al matrix. So far 12 orientations have been reported [7,15,16,17,18]. This implies that interfaces are very important for the η-phase stability. In the case of η'/η_2, which have plate morphology with $(0001)_\eta \parallel (111)_{Al}$ habit plane, the interface layers are one $\{111\}_{Al}$ lattice plane enriched in solute atoms at each side of the precipitate [19,20]. The η_1 phase is a plate with $(10\bar{1}0)_\eta \parallel (001)_{Al}$ habit plane [21]. Needles also exist along $\langle 112\rangle_{Al}$ which do not fall into any previously reported orientation relationship [22]. Observations along the $\langle 110\rangle_{Al}$ zone axis revealed that the η phases precipitating with $[11\bar{2}0]_\eta$ parallel to $[110]_{Al}$, are also bounded by $(1\bar{1}3)_{Al}$ planes defining a new orientation relationship, η_{12} [18]. Recent investigations gave example of other unreported orientation: $[11\bar{2}0]_\eta \parallel [110]_{Al}$, $(\bar{1}100)_\eta \parallel (2\bar{2}1)_{Al}$ as bounded by interface along the $[1\bar{1}\bar{4}]_{Al}$ direction [9]. Table 1 shows a classification of reported orientation relationships. The η phase may also incorporate Mg_6Zn_7 elongated hexagons in addition to the $MgZn_2$ sub-unit cells [18,21,22,23]. Incorporation of Mg_6Zn_7 elongated hexagons shifts the overall Mg/Zn ratio of the precipitate to over 0.5 and their random arrangements yield η precipitate morphologies with undefined orientation relationships with the Al matrix [23]. Recent investigations raised questions about the number of orientation relationships that the η phase can create with the Al matrix. Complexity of different morphologies and orientation relationships, between the η phase and the Al lattice make it challenging to sort out and classify the precipitates using only low magnification bright field imaging. In this work, bright field imaging, electron diffraction and atomic resolution HAADF-STEM imaging have been used to demonstrate that the η phase creates an additional orientation relationship with the Al lattice. Based on the experimental results, an atomic model of the interface was built and refined using first-principles calculations.

Experimental procedure

Four alloys were investigated. These are, with compositions in at. %, Al-3.4Zn-1.9Mg (ZM42), Al-3.4Zn-1.9Mg-1Cu (ZM42HC), Al-2.6Zn-1Mg (ZM31), Al-2.7Zn-2.2Mg-0.29Si-0.22Cu (ZM33SC). The alloys were homogenized at 470 °C for 24h, extruded at 390-405°C and solution heat treated at 475°C for 1 h followed by quenching. Artificial ageing at 150 and 200 °C was immediately carried out following quenching. TEM disks were punched out from ~ 60 µm thick foils and electropolished in a twin-jet polishing machine, using a solution of 1/3 nitric acid (HNO_3) and 2/3 methanol (CH_3OH) kept at a temperature range between -20 and -30 ℃. Observations of the aged Al microstructures were carried out in two different transmission electron microscopes, a 120kV accelerating voltage Topcon EM-002B and a 200kV accelerating voltage double aberration-corrected (image and probe Cs) cold-FEG Jeol ARM-200CF. The high resolution HAADF-STEM images in the latter microscope were recorded with a probe size of 0.08 nm, 28 mrad convergence semi-angle and 35 and 159 mrad inner and outer collection angles, respectively. Smart Align was used to obtain the images in

Fig. 2 (c), (d) and Fig. 4 (a), (b), which involves acquiring a stack of successive low-dose images and afterwards aligning them to correct for rigid- and non-rigid scan distortions [25]. The HAADF-STEM image intensity signal is almost proportional to Z^2 of atoms composing atomic columns providing the advantage of easily distinguishing between atomic columns enriched in heavy and light elements [26].

First-principles calculations were conducted within the Density Functional Theory (DFT) framework using the Vienna ab-initio simulation package (VASP) [27,28] with the Perdew–Burke–Ernzerhof generalized gradient approximation exchange-correlation density functional [29]. The Brillouin-zone *k*-point samplings were chosen using the Monkhorst–Pack algorithm [30]. In this algorithm, 2 × 5 × 1 gamma-centered *k*-point samplings were used for the interface model. The $[2\bar{1}\bar{1}0]$ and $[01\bar{1}0]$ directions were set as the *y* and *x* directions, respectively. The model contains 416 atoms (152 Zn, 64 Mg and 200 Al) confined to $(2\bar{1}\bar{1}0)_{MgZn2} \parallel (001)_{Al}$ = 8:5, $(01\bar{1}0)_{MgZn2} \parallel (120)_{Al}$ = 2:5, $(0001)_{MgZn2}$ = 2, $(\bar{2}10)_{Al}$ = 10 and a vacuum layer width of 1.8 nm. A plane-wave energy cutoff of 400 eV was considered with a first order Methfessel–Paxton scheme employing a smearing parameter of 0.1 eV. The total energy was converged within 10^{-6} eV/atom for all calculations. The relaxed configurations were obtained from the conjugate gradient method that terminated the search when the force on all atoms was reduced to 0.005 eV/Å.

Results

Bright field images of the microstructure of the ZM31 alloy peak-aged at 200 °C for 1,000 min are shown in Fig. 1 (a) and (b). Precipitates of mainly plate and coarse rectangular shaped morphologies were observed. Edge-on projection of plates with habit plane on $\{100\}_{Al}$, most probably η_1 phase are indicated with white arrows. They constitute the primary precipitate morphologies, as the observation zone axis is along $[001]_{Al}$. The second most observed are the cuboid-like precipitates with interfaces bound by $\{110\}_{Al}$ planes and curved corners, as confined by the black arrows in Fig. 1 (a) and (b). This morphology is reported as η phase with the following orientation relationship: $(0001)_{\eta} \parallel (010)_{Al}$ and $(10\bar{1}0)_{\eta} \parallel (001)_{Al}$ and it is listed in tab. 1 [24]. Additional precipitates with $\{120\}_{Al}$ habit planes are indicated with blue arrows. This orientation has not been reported previously and will be named η_{13} in the present work. The orientation is confirmed by electron diffraction and is indicated by the dashed blue lines in the respective electron diffractions patterns seen in the insets of Fig. 1 (a) and (b). For every one of three $\langle 100\rangle_{Al}$ direction, there are four $\{120\}_{Al}$ habit planes. Therefore, there will be 12 equivalent $\{120\}_{Al}$ in which the precipitates can reside. The plates residing on $\{120\}_{Al}$ planes will cause streaking or row of sharp reflections perpendicular to these planes in reciprocal space due to break of periodicity of Al atomic planes in these directions [31]. The electron diffraction pattern of Fig. 1 (d), is obtained from a larger area than that shown in Fig. 1 (c). The typical cross-like reflections of precipitate spots around $\{110\}_{Al}$ forbidden reflections are due to the commonly observed orientation relationships η_1, η_2 and T'(T) phases [15,32]. Unreported rows of reflection spots indicated by the blue arrows in Fig. 1 (d) imply for a particular orientation relationship that creates disturbed atomic distribution in planes perpendicular to that particular Al matrix direction.

The atomic-scale $\langle 100\rangle_{Al}$ zone axis HAADF-STEM image in Fig. 2 (a) shows a precipitate lying on $(210)_{Al}$ plane. The internal structure is built up by stacking of $(0001)_{MgZn2}$ planes parallel with the flat interfaces. The Fast Fourier Transform (FFT) in Fig. 2 (b) shows streaking

of $\langle 0001 \rangle_\eta$ extending from the $(200)_{Al}$ spot to the $(\overline{2}\overline{2}0)_{Al}$. Presence of this typical streaking direction is seen also in the FFTs given in the insets in Fig. 2 (c) and (d).

For better characterization of plates lying on $\{120\}_{Al}$ planes, observations were carried out along $[\overline{1}20]_{Al}$ as confirmed by electron microdiffraction in Fig. 3 (a) and the selected area electron diffraction pattern in Fig. 3 (b). A kinematical diffraction pattern simulation is shown in Fig. 3 (c). Fig. 3 (d) shows a bright field image along $\langle 120 \rangle_{Al}$ in which precipitates appear as with spherical shaped morphologies elongated in different directions. This is due to tilting of common residing planes of the precipitates with respect to the incident beam direction. White arrows indicate precipitate projection edge-on on $\{100\}_{Al}$ most probably η_1. Preciptates with fringes parallel to $\{210\}_{Al}$ planes as shown in the inset of Fig. 3 (d) are indicated with blue arrows.

HAADF-STEM investigations carried out along the $[\overline{1}20]_{Al}$ direction are shown in Fig. 4 (a) and (b). Precipitates with $[01\overline{1}0]_\eta$ parallel to $[\overline{1}20]_{Al}$ zone axis lying on the $\{210\}_{Al}$ plane are seen. In this projection several thickening ledges can be seen in both images. The ledges are always ½ η unit cell or 1 Penrose brick in height. Based on above the analysis, an η_{13} orientation relationship and morphology is determined as:

$$(0001)_\eta \parallel (120)_{Al} \text{ and } (2\overline{1}\overline{1}0)_\eta \parallel (001)_{Al}, \text{ plate on } (120)_{Al}$$

The atomic columns composing the thickening ledges are shorter than the ones deep inside the precipitate (Fig.4), therefore the atomic columns next to the Al lattice yield lower intensity and look like they are gradually blending with the Al atomic columns of surrounding matrix as seen in Fig. 5.

Discussion

The orientation relationships between the precipitates and the matrix in which they are embedded are influenced by the driving force for minimization of interfacial energy. Preservation of coherency/semi-coherency by an almost exact inter atomic rows distance match along the interphase boundaries is a prerequisite for interfacial energy minimization **[33,34]**. Fig. 5 (b) shows the $(\overline{2}\overline{1}0)_{Al} \parallel (0001)_\eta$ interface of the Al lattice / η-phase under the coinciding zone axes $[001]_{Al} \parallel [2\overline{1}\overline{1}0]_\eta$. A coordinate system is applied with respect to η-phase direction indices, in which $[01\overline{1}0]_\eta$ - x and $[2\overline{1}\overline{1}0]_\eta$ - y axes are parallel to the interface plane and 90° to one-another, respectively. Considering a rigid crystal case, and for the x-direction the spacing between planes containing high linear density (or equivalently low linear density) Zn atomic columns of the $MgZn_2$ structure, we have $d_{(01\text{-}10)\eta} = 0.452$ nm, which exactly matches the Al atomic columns spaced with d-value of $2.5*d_{(1\text{-}20)Al} = 0.451$ nm as illustrated in Fig. 5 (c). The precipitate is rotated 26.5° from the $\{100\}_{Al}$ planes in order to achieve a minimum d-value mismatch between matching planes as illustrated in Fig. 6 (a). A large d-value mismatch requires a large angle of rotation of the matching planes in order to compensate for the differences in the interplanar spacing **[35,36].** For full characterization of the interfacial planar misfit, the misfit was calculated for the y-direction. In order to achieve maximum atomic matching, the coinciding lattice sites in which periodically the atoms fall onto almost the same positions should be maximal or the periodic distance over which it occurs should be minimal **[37,38,39]**. Considering rigid atomic positioning of η_{13} and the Al lattice along the y-direction, Zn atoms are successively spaced along low linear density Zn atomic columns with the unit

cell parameter of the $MgZn_2$ phase, $2d_{(2\text{-}1\text{-}10)\eta} = a_\eta = 0.52$ nm and along the high-density Zn with $d_{(2\text{-}1\text{-}10)\eta} = 0.26$ nm as illustrated in Fig. 6 (b). The Al atoms are spaced with $d_{(001)Al} = 0.404$ nm. Considering that for Al atoms every 5th $d_{(001)Al} = 2.022$ nm will fall near to Zn atoms of $8d_{(2\text{-}1\text{-}10)\eta} = 2.1$ nm (low or high density columns, respectively) the interface rigid model was relaxed to 2.043 nm along y-direction, 1% expansion of $5d_{(001)Al}$ and -2.7% contraction of $8d_{(2\text{-}1\text{-}10)\eta}$ as illustrated in the fully relaxed model in Fig. 6 (c). Relaxation of the model introduced interfacial dislocation in the Al lattice after $5d_{(002)Al}$ interplanar spacings along the y-direction, as seen in Fig. 6 (c). Interfacial dislocation spacing will periodically relax the strain generated by the increased misfit every $10d_{(002)Al}$. Zn atoms along the high-density Zn atomic columns and Al atoms over low density Zn atomic columns will experience the highest shifts upon the relaxation, as clearly seen in the relaxed interface model.

Directional misfit may explain the thickening ledges which are not fully grown along the y-direction and the fully development along x-direction. The higher number of incomplete ledges along the y-direction may be related to the high misfit between the $(002)_{Al}$ and $(2\bar{1}\bar{1}0)_\eta$ planes. Meanwhile, the absence of stepped ledges along x-direction can be due to the perfect fit between planes perpendicular to the x-direction. The absence of stepped thickening ledges along the x-direction is confirmed in several $\langle 100\rangle_{Al}$ zone axis images of η_{13} seen in Fig. 2. Meanwhile the presence of multiple step ledges on η_{13} is confirmed in images taken along $\langle 120\rangle_{Al}$ zone axis as seen in Fig. 4.

Misfit dislocations at the η_{13} relaxed interface is due to relaxation of increased strain generated by the misfit between the precipitate and matrix atomic planes perpendicular to the y-direction. Interfacial dislocation cores should serve as nucleation centers for thickening ledges and at the same time preventing ledge growth along the y-direction parallel to the interface plane. The later will be impeded by the periodic distribution of interfacial dislocations and their generated strain fields. The moment the ledge will grows more than 2 successive interfacial dislocations along the y-direction, a new interfacial dislocation will be generated on top of the thickening ledge, which in turn will serve as a new nucleation center. It can be assumed that after nucleation of the thickening ledges on the $(0001)_{\eta 13}$ interface, they grow faster parallel to the $\langle 120\rangle_{Al}$ direction (x-direction) than to $\langle 001\rangle_{Al}$ direction (y-direction). This assumption is strongly supported by the relaxed interfacial model shown in Fig. 6 (c) and the observed results. The directional misfit should affect the directional growth rate of the thickening ledges, which will be highest in the direction of the lowest misfit. The relaxed interfacial model falls into good agreement with the multi-step thickening ledges observed along the y-direction as seen in Fig. 4.

Conclusions

Transmission electron microscopy imaging, electron diffraction and scanning transmission electron microscopy were employed for characterization of nanoscale precipitates in a number of Al-Zn-Mg based alloys. A new orientation relationship was identified between the η - $MgZn_2$ precipitate and the Al matrix in alloys mainly aged at ≥ 150°C. The η_{13} orientation relationship is $(0001)_\eta \parallel (120)_{Al}$ and $(2\bar{1}\bar{1}0)_\eta \parallel (001)_{Al}$, plate on $\{120\}_{Al}$. Projection of the precipitate interface along two aluminum zone axes revealed that the thickening ledges were significantly stepped along the direction with the highest misfit. Relaxation of the interface

model build upon acuired images falls into good agreement with experimental results and fairly well explains the anisotropy of the growth rate of thicknening ledges along diferent directions.

Acknowledgement

The authors acknowledge JST (Japan Science and Technology Agency) under collaborative research based on industrial demand “Heterogeneous Structure Control”: Toward innovative development of metallic structural materials (Grant Number #20100114), Light Metal Educational Foundation, President description, University of Toyama (2018-2019), INTPART the Research Council of Norway through the project (249698) and the NORTEM project (197405). The authors also thank to Dr. S. Lee and Dr. T. Tsuchiya for ingot castings and Dr. S. Murakami and Mr. T. Yoshida of Aisin Keikinzoku Co., Ltd. (Imizu, Toyama, Japan) for analysis of chemical composition of alloy ingots.

The raw/processed data required to reproduce these findings cannot be shared at this time due to technical or time limitations.

References

[1] T. Dursun, C. Soutis, Recent developments in advanced aircraft aluminium alloys, Mater. Des., 56 (2014), pp. 862-871. doi:10.1016/j.matdes.2013.12.002

[2] D.A. Porter, K.E. Easterling, Phase Transformations in Metals and Alloys, Second Edition (1992).

[3] L.K. Berg, J. Gjønnes, V. Hansen, X.Z. Li, M. Knutson-Wedel, G. Waterloo, D. Schryvers, L.R. Wallenberg, GP-zones in Al-Zn-Mg alloys and their role in artificial ageing, Acta Mater., 49 (2001), pp. 3443-3451. doi:10.1016/S1359-6454(01)00251-8

[4] K. Matsuda, A. Kawai, K. Watanabe, S. Lee, C.D. Marioara, S. Wenner, K. Nishimura, T. Matsuzaki, N. Nunomura, T. Sato, R. Holmestad, S. Ikeno, Extra Electron Diffraction Spots Caused by Fine Precipitates Formed at the Early Stage of Aging in Al-Mg-X (X=Si, Ge, Zn)-Cu Alloys, Mater. Trans., 58 (2) (2017), pp. 167-175. doi:10.2320/matertrans.L-M2016839

[5] J. Buha, R.N. Lumley, A.G. Crosky, Secondary ageing in an aluminium alloy 7050, Mater. Sci. Eng., A492 (2008), pp. 1-10. doi:10.1016/j.msea.2008.02.039

[6] V. Hansen, O.B. Karlsen, Y. Langsrud, J. Gjønnes, Precipitates, zones and transitions during ageing of Al-Zn-Mg-Zr 7000 series alloy, Mater. Sci. Tech., 20 (2) (2004), pp. 185-193. doi:10.1179/026708304225010424

[7] J. Gjønnes, Chr.J. Simensen, An Electron Microscope Investigation of the Microstructure in an Aluminium-Zinc-Magnesium Alloy, Acta Metall., 18 (1970), pp. 881-890. doi:10.1016/0001-6160(70)90016-7

[8] N. Ryum, Precipitation Kinetics in an Al-Zn-Mg Alloy, Z. Metallkunde, 66 (1975), pp. 338-343.

[9] A. Lervik, C.D. Marioara, M. Kadanik, J.C. Walmsley, B. Milkereit, R. Holmestad, Precipitation in an extruded AA7003 aluminum alloy: observations of 6xxx-type hardening phases, Mater. Des. (2019) (in press).

[10] H. Inoue, T. Sato, Y. Kojima, T. Takahashi, The temperature limit for GP zone formation in an Al-Zn-Mg alloy, Metall. Trans. 12A (1981), pp. 1429-1434. doi:10.1007/BF02643687

[11] C.K. Akuata, C. Altenbach, C. Schnatterer, P. Suwanpinij, C. Saiyasombat, D. Zander, Age hardening response of AA7108A investigated by means of Synchrotron-based X-ray Absorption Spectroscopy (XAS) measurements, Mater. Sci. Eng., A747 (2019), pp. 42-52. doi:10.1016/j.msea.2019.01.052

[12] R.M. Allen, J.B. Vander Sande, The oriented growth of precipitates on dislocations in Al-Zn-Mg–part I. Experimental observations, Acta Metall., 28 (1980), pp. 1185-1195. doi:10.1016/0001-6160(80)90073-5

[13] J.B. Friauf, The Crystal Structure of Magnesium Di-Zincide, Phys. Rev., 29 (1927), pp. 34-40.

[14] Y. Komura, K. Tokunaga, Structural Studies of Stacking Variants in Mg-Base Friauf-Laves Phases, Acta Cryst., B36 (1980), pp. 1548-1554. doi:10.1107/S0567740880006565

[15] P.A. Thackery, The Nature and Morphology of Precipitate in Al-Zn-Mg Alloys, J. Inst. Met., 96 (1968), pp. 228-235.

[16] H. Löffler, I. Kovács, J. Lendvai, Decomposition processes in Al-Zn-Mg alloys, J. Mater. Sci. 18 (1983) 2215-2240. doi:10.1007/BF00541825

[17] H.P. Degischer, W. Lacom, A. Zahra, C.Y. Zahra, Decomposition Processes in an Al-5% Zn-1% Mg Alloy, PZ. Metallkde, 71(4) (1980), pp. 231-238.
[18] T.F. Chung, Y.L. Yang, M. Shiojiri, C.N. Hsiao, W.C. Li, C.S. Tsao, Z. Shi, J. Lin, J.R. Yang, An atomic scale structural investigation of nanometer-sized η precipitates in the 7050 aluminium alloy, Acta Mater., 174 (2019), pp. 351-368. doi:10.1016/j.actamat.2019.05.041
[19] C.D. Marioara, W. Lefebvre, S.J. Andersen, J. Friis, Atomic structure of hardening precipitates in an Al-Mg-Zn-Cu alloy determined by HAADF-STEM and first-principles calculations: relation to η-$MgZn_2$, J. Mater. Sci., 48 (2013), pp. 3638-3651. doi:10.1007/s10853-013-7158-3
[20] Y. Li, L. Kovarik, P.J. Philips, Y. Hsu, W. Wang, M.J. Mills, High-resolution characterization of the precipitation behavior of an Al-Zn-Mg-Cu alloy, Philos. Mag. Lett. 92 (4) (2012), pp.166-178. doi:10.1080/09500839.2011.652682
[21] A. Bendo, K. Matsuda, S. Lee, K. Nishimura, N. Nunomura, H. Toda, M. Yamaguchi, T. Tsuru, K. Hirayama, K. Shimizu, H. Gao, K. Ebihara, M. Itakura, T. Yoshida, S. Murakami, Atomic scale HAADF-STEM study of η' and η_1 phases in peak-aged Al-Zn-Mg alloys, J. Mater. Sci., 53 (2018), pp. 4598-4611. doi:10.1007/s10853-017-1873-0
[22] S.J. Andersen, C.D. Marioara, J. Friis, S. Wenner, R. Holmestad, Precipitates in aluminium alloys, Adv. Phys. X., 3 (1) (2018), pp. 790-813. doi:10.1080/23746149.2018.1479984
[23] A. Bendo, T. Maeda, K. Matsuda, A. Lervik, R. Holmestad, C.D. Marioara, K. Nishimura, N. Nunomura, H. Toda, M. Yamaguchi, K. Ikeda, T. Homma, Characterisation of structural similarities of precipitates in Mg-Zn and Al-Zn-Mg alloys systems, Phil. Mag. 0 (2019), pp. 1-17. doi:10.1080/14786435.2019.1637032
[24] A. Deschamps, Y. Brechet, Nature and Distribution of quenched-induced precipitation in an Al-Zn-Mg-Cu alloy, Scr. Mater., 39 (11) (1998), pp. 1517-1522. doi:10.1016/S1359-6462(98)00357-1
[25] L. Jones, H. Yang, T.J. Pennycook, M.S.J. Marshall, S.V. Aert, N.D. Browing, M.R. Castell, P.D. Nellist, Smart Align – a new tool for robust non-rigid registration of scanning microscope data, Adv. Struct. Chem. Imaging, 1 (8) (2015), pp. 1-16. doi:10.1186/s40679-015-0008-4
[26] P.D. Nellist, S.J. Pennycook, The principles and interpretation of annular dark-field Z-contrast imaging, Adv. Imag. Elect. Phys., 113 (2000), pp. 147-203. doi:10.1016/S1076-5670(00)80013-0
[27] G. Kresse, J. Hafner, Ab initio molecular dynamics for liquid metals, Phys. Rev., B 47 (1993), pp. 558–561. doi:10.1103/PhysRevB.47.558
[28] G. Kresse, J. Furthmuller, Efficient iterative schemes for ab initio total-energy calculations using a plane-wave basis set, Phys. Rev., B 54 (1996), pp. 11169–11186. doi:10.1103/PhysRevB.54.11169
[29] J.P. Perdew, K. Burke, M. Ernzerhof, Generalized Gradient Approximation Made Simple, Phys. Rev. Lett., 77 (1996), pp. 3865-3868. doi:10.1103/PhysRevLett.77.3865
[30] H.J. Monkhorst, J.D. Pack, Special points for Brillouin-zone integrations, Phys. Rev., B 13 (1976), pp. 5188–5192. doi:10.1103/PhysRevB.13.5188
[31] J.B. Newkirk, R. Smoluchowski, A.H. Geisler, D.L. Martin, Diffuse Scattering by an Ordering Alloy, Acta Mater., 4 (1951), pp. 507-512. doi:10.1107/S0365110X51001720

[32] K. Matsuda, T. Yasumoto, A. Bendo, T. Tsuchiya, S. Lee, K. Nishimura, N. Nunomura, C.D. Marioara, A. Lervik, R. Holmestad, H. Toda, M. Yamaguchi, K. Ikeda, T. Homma, S. Ikeno, Effect of Copper Addition on Precipitation Behavior near Grain Boundary in Al-Zn-Mg alloy, Mater. Trans. 60 (8) (2019), pp. 1688-1696. doi:10.2320/matertrans.L-M2019828
[33] G.J. Shiflet, J.H. Van Der Merwe, The Role of Structural Ledges as Misfit-Compensating Defects: fcc-bcc Interphase Boundaries, Metall. Mater. Trans., 25A (1994), pp. 1895-1903. doi:10.1007/BF02649037
[34] G.J. Shiflet, J.H. Van Der Merwe, Misfit accommodation by steps in cubic materials, J. Electron Mater., 20(10) (1991), pp. 785-791. doi:10.1007/BF02665966
[35] M.X. Zhang, P.M. Kelly, Edge-to-edge matching model for prediction orientation relationships and habit planes – the improvements, Scr. Mater., 52 (2005), pp. 963-968. doi:10.1016/j.scriptamat.2005.01.040
[36] M.X. Zhang, P.M. Kelly, Crystallographic study of grain refinement in aluminum alloys using the edge-to-edge matching model, Acta Mater., 53 (2005), pp. 1073-1084. doi:10.1016/j.actamat.2004.11.037
[37] J. Yang, J.L. Wang, Y.M. Wu, L.M. Wang, H.J. Zhang, Extended application of edge-to-edge matching model to HCP/HCP (α-Mg/$MgZn_2$) system in magnesium alloys, Mater. Sci. Eng., A460-461 (2007), pp. 296-300. doi:10.1016/j.msea.2007.01.097
[38] M.X. Zhang, P.M. Kelly, M.A. Easton, J.A. Taylor, Crystallographic study of grain refinement in aluminum alloys using the edge-to-edge matching model, Acta Mater., 53 (2005), pp. 1427-1438. doi:10.1016/j.actamat.2004.11.037
[39] P.M. Kelly, M.X. Zhang, Edge-to-Edge Matching – The Fundamentals, Metall. Mater. Trans., 37A (2006), pp. 833-839. doi:10.1007/s11661-006-0056-4
[40] F.C. Frank, J.S. Kasper, Complex Alloy Structures Regarded as Sphere Packings I. Definitions and Basic Principles, Acta Cryst., 11 (1958), pp. 184-190. doi:10.1107/S0365110X58000487

	Orientation relationship		Morphology	References
η_2	$(0\,0\,0\,1)_\eta \parallel (1\,\bar{1}\,\bar{1})_{Al}$	$(1\,0\,\bar{1}\,0)_\eta \parallel (1\,1\,0)_{Al}$	plate on $\{111\}_{Al}$	P.A. Thackery [15]
η_3	$(0\,0\,0\,1)_\eta \parallel (1\,\bar{1}\,\bar{1})_{Al}$	$(1\,1\,\bar{2}\,0)_\eta \parallel (1\,1\,0)_{Al}$	plate on $\{111\}_{Al}$	N. Ryum [8]
η_{10}	$(0\,0\,0\,1)_\eta \parallel (1\,\bar{1}\,\bar{1})_{Al}$	$(1\,1\,\bar{2}\,0)_\eta \parallel (1\,\bar{3}\,4)_{Al}$		H. Löffler *et al.* [16]
η_1	$(0\,0\,0\,1)_\eta \parallel (1\,1\,0)_{Al}$	$(1\,0\,\bar{1}\,0)_\eta \parallel (0\,0\,1)_{Al}$	plate on $\{001\}_{Al}$	P.A. Thackery [15]
η_9	$(0\,0\,0\,1)_\eta \parallel (1\,1\,0)_{Al}$	$(1\,1\,\bar{2}\,0)_\eta \parallel (0\,0\,1)_{Al}$	plate on $\{001\}_{Al}$	H.P. Degischer *et al.* [17]
η_{11}	$(0\,0\,0\,1)_\eta \parallel (1\,1\,0)_{Al}$	$(1\,0\,\bar{1}\,0)_\eta \parallel (1\,\bar{1}\,\bar{1})_{Al}$		H.P. Degischer *et al.* [17]
η_4	$(1\,1\,\bar{2}\,0)_\eta \parallel (1\,\bar{1}\,\bar{1})_{Al}$	$(0\,0\,0\,1)_\eta \parallel (1\,1\,0)_{Al}$	rod/lath on $\{111\}_{Al}$	P.A. Thackery [15]
η_5	$(1\,1\,\bar{2}\,0)_\eta \parallel (1\,\bar{1}\,\bar{1})_{Al}$	11° to $\langle 110\rangle_{Al}$	rod/lath on $\{111\}_{Al}$	P.A. Thackery [15]
η_6	$(1\,1\,\bar{2}\,0)_\eta \parallel (1\,\bar{1}\,\bar{1})_{Al}$	15° to $\langle 110\rangle_{Al}$	rod/lath on $\{111\}_{Al}$	P.A. Thackery [15]
η_7	$(1\,1\,\bar{2}\,0)_\eta \parallel (1\,\bar{1}\,\bar{1})_{Al}$	25° to $\langle 110\rangle_{Al}$	rod/lath on $\{111\}_{Al}$	P.A. Thackery [15]
η_8	$(1\,1\,\bar{2}\,0)_\eta \parallel (1\,\bar{1}\,2)_{Al}$	$(0\,0\,0\,1)_\eta \parallel (3\,1\,\bar{1}\,)_{Al}$	rod along $\langle 112\rangle_{Al}$	J. Gjønnes *et al.* [7]
η_{12}	$(1\,1\,\bar{2}\,0)_\eta \parallel (1\,1\,0)_{Al}$	$(0\,0\,0\,1)_\eta \parallel (1\,\bar{1}\,3)_{Al}$	on $\{1\bar{1}3\}_{Al}$	T.F. Chung *et al.* [18]
η	$(1\,1\,\bar{2}\,0)_\eta \parallel (1\,1\,0)_{Al}$	$(\bar{1}\,1\,0\,0)_\eta \parallel (2\,\bar{2}\,1)_{Al}$	on $\{2\bar{2}1\}_{Al}$	A. Lervik *et al.* [9]
η	$(0\,0\,0\,1)_\eta \parallel (0\,1\,0)_{Al}$	$(1\,0\,\bar{1}\,0)_\eta \parallel (0\,0\,1)_{Al}$	bounded by $\{110\}_{Al}$	A. Deschamps *et al.* [24]

Tab. 1 The 12 reported orientation relationships of $MgZn_2$ phase with Al matrix sorted according to their orientation relationships. Morphologies are indicated. The notations used according to Gjønnes *et al.* [7].

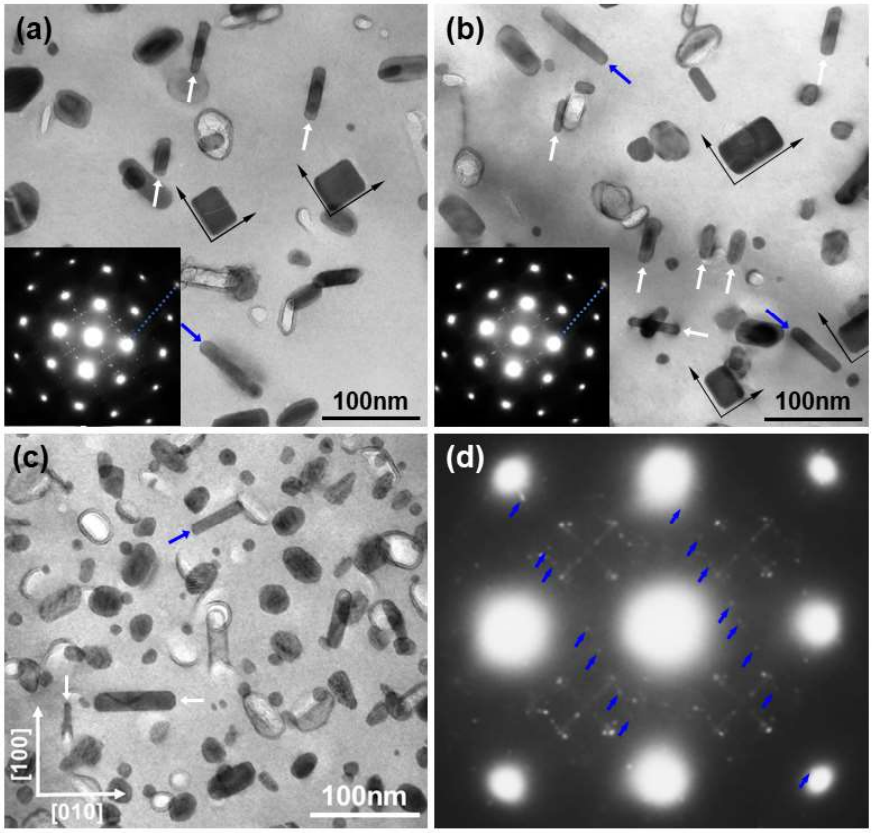

Fig. 1 (a), (b) TEM images along $[001]_{Al}$ in the ZM31 alloy peak-aged at 200 °C for 1.000 min and corresponding electron diffraction given in the insets. (c) TEM image along $[001]_{Al}$ in the ZM42HC alloy over-aged at 200 °C for 400 min and (d) its corresponding electron diffraction in which the blue arrows indicate rows of spots along $[\bar{2}10]_{Al}$. White, black and blue arrows show precipitate interfaces bounded by $\{100\}_{Al}$, $\{110\}_{Al}$ and $\{120\}_{Al}$ planes, respectively.

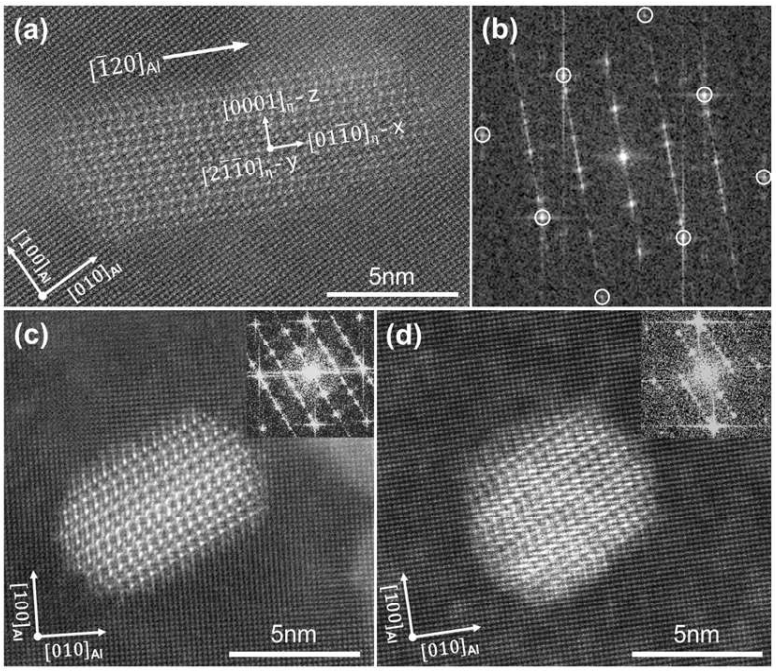

Fig. 2 (a) $[001]_{Al}$ HAADF-STEM image of precipitate in ZM33SC alloy peak-aged at 150 °C for 1,000 min with (b) corresponding FFT. (c), (d) Smart aligned $[001]_{Al}$ HAADF-STEM images of precipitate in ZM42 peak-aged at 150 °C for 400 min and corresponding FFT given in insets.

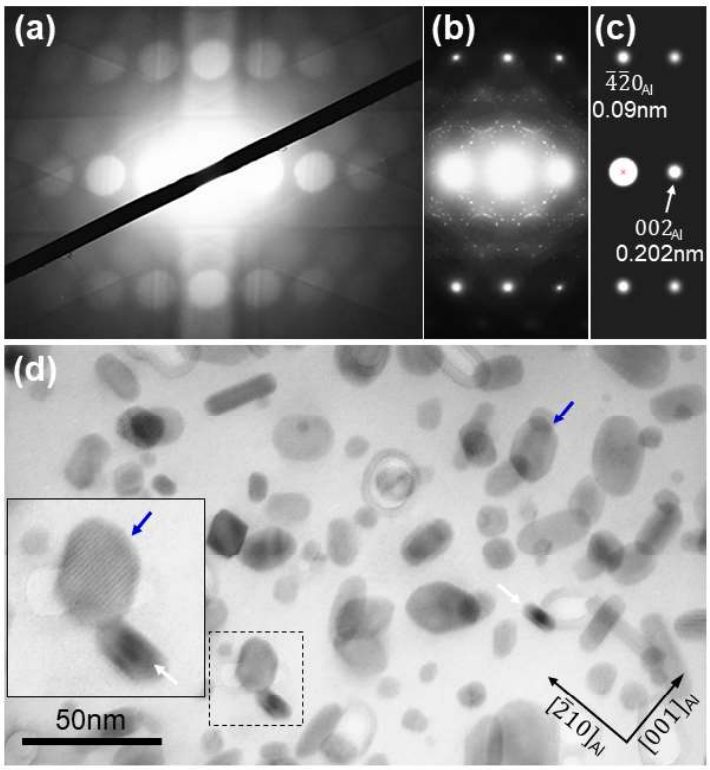

Fig. 3 $\langle 120 \rangle_{Al}$ zone axis (a) electron microdiffraction (b) selected area electron diffraction (c) simulated kinematic electron diffraction and (d) bright field image in alloy ZM42 over-aged at 150°C for 10,000 min.

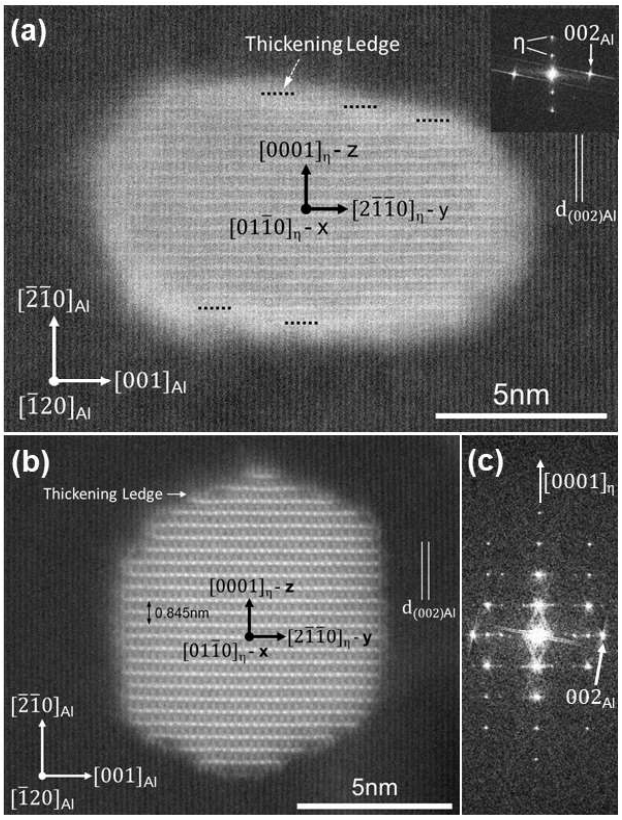

Fig. 4 (a), (b) Smart aligned HAADF-STEM images of edge-on precipitates on $\{210\}_{Al}$ plane in the $[\bar{1}20]_{Al}$ axis in alloy ZM42 over-aged at 150°C for 10,000 min and (c) corresponding FFT of image (b).

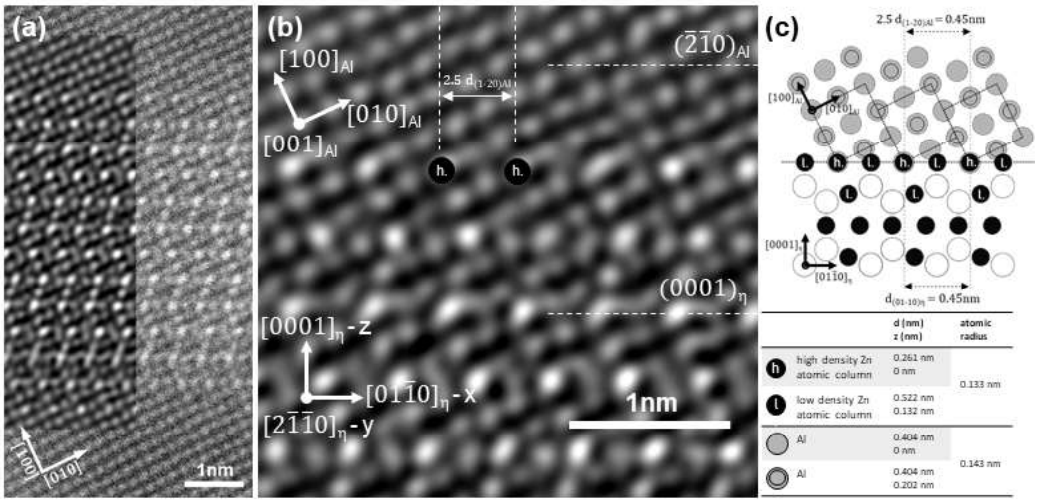

Fig. 5 (a) Magnified section of the precipitate in Fig. 2 (a) in which a Fourier Filtered image is included. (b) Noise suppressed IFFT image of the η_{13}/Al interface. (c) Schematic illustration of the atomic configuration along the interface. The table indicates periodic distance of atoms along the column parallel with the observation direction, d (nm) and the height of atoms off the basal plane, z (nm).

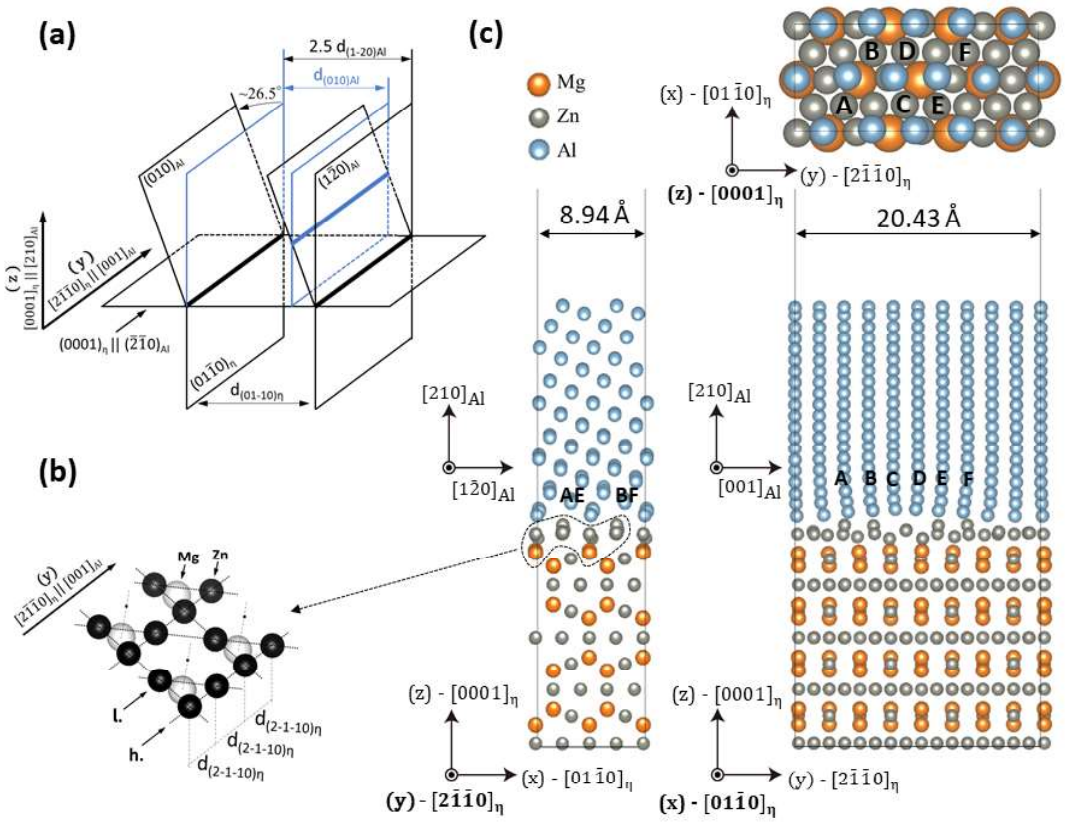

Fig. 6 (a) Illustration of plane matching between $\{010\}_{Al}$ and $(01\bar{1}0)_{\eta}$ planes. For achieving perfect match between Al and $MgZn_2$ planes, $(01\bar{1}0)_{\eta}$ planes are tilted ~26.5° from $\{010\}_{Al}$ planes. Consequently, the interplanar matching misfits along the x-direction is reduced from ~11.9% to ~0.12%. Indicies are based on the hexagonal unit cell reference of $MgZn_2$ phase. (b) Kagome net arrangement of Zn atoms **[40]** and inter-atomic spacing between succesive Zn atoms along low and high density Zn atomic columns (y-direction). (c) The fully relaxed interface model along $[2\bar{1}\bar{1}0]_{\eta}$, $[01\bar{1}0]_{\eta}$ and $[0001]_{\eta}$ directions.